remote sensing

MDPI

Article

Assessing the Potential of Geostationary Satellites for Aerosol Remote Sensing Based on Critical Surface Albedo

Xavier Ceamanos [1,*], Suman Moparthy [1], Dominique Carrer [1] and Felix C. Seidel [2]

[1] CNRM, Université de Toulouse, Météo-France, CNRS, 42 avenue Gaspard Coriolis, 31057 Toulouse, France; suman.moparthy@meteo.fr (S.M.); dominique.carrer@meteo.fr (D.C.)

[2] Jet Propulsion Laboratory, California Institute of Technology, 4800 Oak Grove Dr, Pasadena, CA 91109, USA; felix.c.seidel.caprez@jpl.nasa.gov

* Correspondence: xavier.ceamanos@meteo.fr

Received: 15 November 2019; Accepted: 9 December 2019; Published: 10 December 2019

check for updates

Abstract: Geostationary satellites are increasingly used for the detection and tracking of atmospheric aerosols and, in particular, of the aerosol optical depth (AOD). The main advantage of these spaceborne platforms in comparison with polar orbiting satellites is their capability to observe the same region of the Earth several times per day with varying geometry. This provides a wealth of information that makes aerosol remote sensing possible when combined with the multi-spectral capabilities of the on-board imagers. Nonetheless, the suitability of geostationary observations for AOD retrieval may vary significantly depending on their spatial, spectral, and temporal characteristics. In this work, the potential of geostationary satellites was assessed based on the concept of critical surface albedo (CSA). CSA is linked to the sensitivity of each spaceborne observation to the aerosol signal, as it is defined as the value of surface albedo for which a varying AOD does not alter the satellite measurement. In this study, the sensitivity to aerosols was determined by estimating the difference between the surface albedo of the observed surface and the corresponding CSA (referred to as dCSA). The values of dCSA were calculated for one year of observations from the Meteosat Second Generation (MSG) spacecraft, based on radiative transfer simulations and information on the satellite acquisition geometry and the properties of the observed surface and aerosols. Different spectral channels from MSG and the future Meteosat Third Generation-Imager were used to study their distinct capabilities for aerosol remote sensing. Results highlight the significant but varying potential of geostationary observations across the observed Earth disk and for different time scales (i.e., diurnal, seasonal, and yearly). For example, the capability of sensing multiples times during the day is revealed to be a notable strength. Indeed, the value of dCSA often fluctuates significantly for a given day, which makes some instants of time more suitable for aerosol retrieval than others. This study determines these instants of time as well as the seasons and the sensing wavelengths that increase the chances for aerosol remote sensing thanks to the variations of dCSA. The outcomes of this work can be used for the development and refinement of AOD retrieval algorithms through the use of the concept of CSA. Furthermore, results can be extrapolated to other present-day geostationary satellites such as Himawari-8/9 and GOES-16/17.

Keywords: aerosols; remote sensing; geostationary satellites; AOD; critical surface albedo; radiative transfer; Meteosat

1. Introduction

Reliable information on the spatial coverage and temporal evolution of aerosols is key for studies on weather forecast, climate, air quality, and air transportation [1]. Global and regional maps of the rapidly changing properties of these atmospheric particles are nowadays made available thanks to the combination of spaceborne remote sensing and suitable retrieval algorithms. On the one hand, satellites equipped with multi-spectral imagers provide information at multiple geometries and wavelengths across space and time. This wealth of information allows imagers to detect the characteristic directional, spectral, and temporal signatures of aerosol particles. On the other hand, retrieval methods are devised to exploit these features with the goal of estimating aerosol properties such as the aerosol optical depth (AOD) [2]. However, aerosol remote sensing may become challenging in some cases when observations do not provide enough contrast between the observed aerosols and the underlaying surface [3]. The coupling at the satellite level between these two elements of the atmosphere–surface system represents the main obstacle for aerosol (and surface) remote sensing in the visible and near-infrared ranges. The success in retrieving accurate estimates of AOD; therefore, strongly depends on the variety of the information acquired by the satellites.

Recently, geostationary satellites have gained prominent interest for aerosol studies [4–7]. The main reason is that this type of spacecrafts provides a wealth of multi-varied information thanks to the sensing of a same region of the Earth multiple times during the day and during the year. This is possible thanks to the high temporal resolution of the on-board imagers and the motion of the Sun with respect to the satellite, which is otherwise immobile with respect to the Earth. Among the current meteorological geostationary satellites, we find the Meteosat Second Generation (MSG) platform from the European Organization for the Exploitation of Meteorological Satellites (EUMETSAT) [8], the Geostationary Operational Environmental Satellites (GOES)-16/17 from the National Oceanic and Atmospheric Administration (NOAA) [9], and the Himawari-8/9 spacecrafts from the Japan Aerospace Exploration Agency (JAXA) [10]. Other examples are the FengYun-2/4 platform operated by China's National Satellite Meteorological Center and the Indian National Satellite System (INSAT)-3DR from the Indian Space Research Organization (ISRO). Regarding the current Meteosat platform, MSG is equipped with the multi-spectral imager Spinning Enhanced Visible and InfraRed Imager (SEVIRI) that scans the Earth disk that is seen from the MSG position at 0° longitude every 15 minutes. The multi-directional and multi-spectral information that is made available by the MSG/SEVIRI platform is combined with its high spatial resolution (i.e., 3 km at the sub-satellite point) to make aerosol retrieval possible. The new generation of geostationary platforms such as Himawari-8/9, GOES-16/17, and the upcoming Meteosat Third Generation-Imager (MTG-I) [11] (launch scheduled for late 2021) brings new capabilities for aerosol remote sensing, principally thanks to their additional sensing wavelengths [12,13].

Nowadays, many retrieval algorithms exist to derive AOD from geostationary satellites [14–26]. Regarding Meteosat, one example is the approach named aerosol and surface albedo retrieval using a directional splitting method-application to geostationary data (AERUS-GEO), which provides daily averaged AOD based on observations from SEVIRI [16,20]. Similar to AERUS-GEO, the majority of the retrieval algorithms do not take into account the different sensitivity to aerosols of the observations that are made available by geostationary imagers. For example, some observations may be related to a higher contrast between the aerosols and the surface thanks to a more favorable acquisition geometry or wavelength. Such favorable observations could be prioritized by inversion algorithms as they are prone to give a more accurate AOD estimate. Contrarily, observations related to unfavorable inversion conditions could be flagged or dealt differently by retrieval methods.

This work provides a tool to tackle these limitations based on the concept of the critical surface albedo (CSA). CSA is linked to the degree of sensitivity to aerosols of a given spaceborne observation, as it is defined as the value of surface albedo that makes the satellite signal insensitive to a varying AOD. An increasing aerosol load over a dark surface (i.e., albedo lower than CSA) will make top-of-atmosphere (TOA) reflectance increase [27]. Conversely, the same situation over a bright surface (i.e., albedo greater than CSA) will make TOA reflectance decrease. When surface albedo is equal to CSA, the TOA reflectance becomes insensitive of the aerosol amount because the increased scattering is counterbalanced by the enhanced attenuation of radiation. In contrast, the sensitivity to the AOD increases with the difference between the surface albedo and the CSA.

Critical surface albedo (or reflectance) was first introduced in the context of aerosol remote sensing by Fraser and Kaufman [28]. Afterwards, some studies exploited the CSA concept to gain information on the optical properties of aerosols [29–31]. A comprehensive study on the CSA and its dependence on the different parameters that play an important role in remote sensing was conducted by Seidel and Popp [32]. Boehmler et al. used the implications of CSA to study the limits of aerosol retrieval over the bright surfaces of Nevada [33]. Recently, some works considered the CSA to study the above-cloud radiative effects of aerosols [34]. Finally, Zhang et al. underlined the loss of accuracy that the retrieval of other atmospheric constituents, namely column-weighted CO_2 mixing ratio, suffers for surfaces close to CSA [35].

The present study extends the work conducted by Seidel and Popp in [32] by investigating the properties of the typical CSA values that correspond to geostationary observations. The difference between the CSA and the albedo of the observed surface (hereafter referred to as dCSA) is calculated to quantify the sensitivity to the AOD. The value of dCSA is finally exploited to determine the potential of geostationary observations for aerosol remote sensing. This study is done across the spatial, temporal, and spectral characteristics of the observations thanks to the dependence of dCSA on the acquisition parameters (i.e., geometry and wavelength) and the properties of the observed surface and aerosols. In particular, the maps of dCSA corresponding to one complete year of Meteosat observations are generated based on radiative transfer simulations and ancillary information. Several channels from the imagers SEVIRI on MSG and the future Flexible Combined Imager (FCI) on MTG-I are considered. The obtained maps of dCSA are used to determine the capabilities of these geostationary platforms for aerosol remote sensing according to the time of the year, the time of the day, the geographic location, and the sensing wavelength. Another result of this study is the derivation of simple equations to allow the scientific community to calculate CSA without the need of performing costly radiative transfer simulations. The outcomes of this study can be useful for the developing of aerosol retrieval algorithms and can be easily extrapolated to other geostationary platforms such as GOES-16/17 or Himawari-8/9.

The article is organized as follows. First, the method to calculate the maps of dCSA for Meteosat are detailed in Section 2. The data used in this work are also described here. The analysis of the obtained results is reported in Section 3. Section 4 discusses the relation between the value of dCSA and the sensitivity to the aerosol signal, as well as the potential implications of the present work for studies on aerosol remote sensing. Finally, conclusions are drawn in Section 5.

2. Methods and Materials

2.1. Overview

The strategy to study the dCSA corresponding to the Meteosat platforms is presented in Figure 1. First, a look-up table (LUT) of satellite-alike values of top-of-atmosphere (TOA) reflectance was built based on radiative transfer simulations for multiple combinations of acquisition geometry, aerosol conditions, and wavelength (see Section 2.2). Second, the LUT of TOA reflectance was used to calculate a second LUT of CSA values (see Section 2.3). Third, the sensor geometry and the ancillary data that were used to define the surface and the aerosols are detailed in Section 2.4. Fourth, Section 2.5 describes the combination of the LUT of CSA and the ancillary data that was carried out to calculate the maps of dCSA corresponding to one year of Meteosat observations.

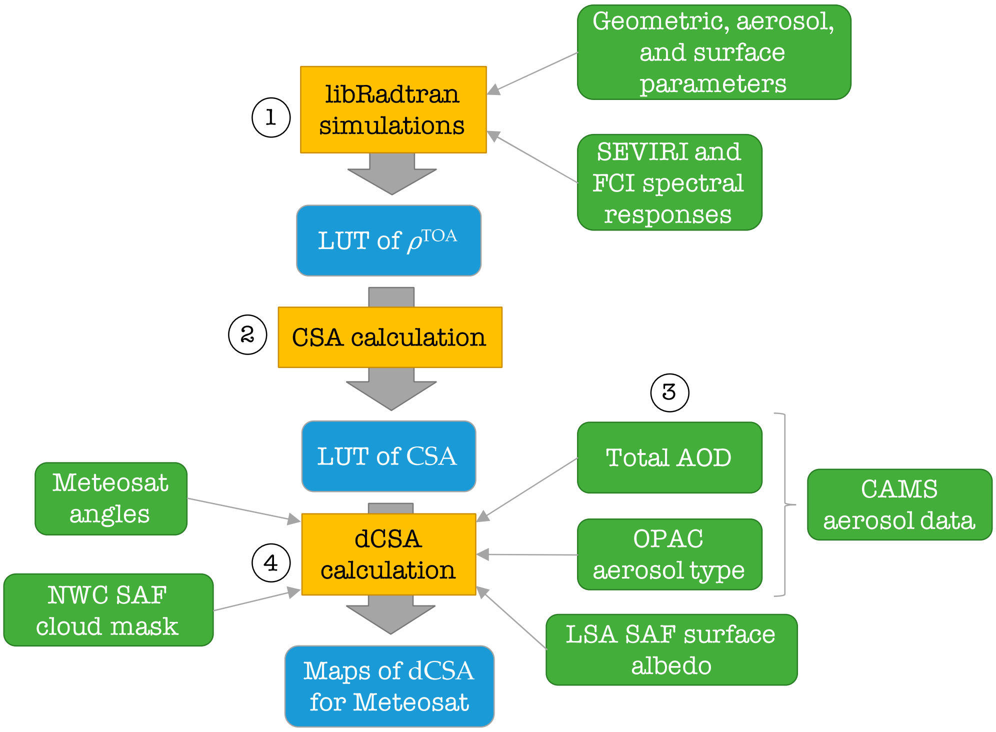

Figure 1. Scheme describing the calculation of the maps of difference between CSA and surface albedo (dCSA) for one full year of Meteosat observations.

2.2. Look-up Table of TOA Reflectance

Values of TOA reflectance were simulated using the radiative transfer code libRadtran [36,37] (see bullet 1 in Figure 1). Simulations were carried out for an extensive range of configurations regarding solar and view geometry, aerosol properties, surface albedo, and wavelength (see Table 1) to encompass the different observations that are made available by geostationary satellites. The acquisition geometry was defined by the solar zenith angle (SZA, θ_s), the view zenith angle (VZA, θ_v), and the relative azimuth angle (RAA, φ). A dense sampling was chosen for surface albedo (a_s) in order to carry out an accurate retrieval of CSA in the following step. Table 1 shows the five spectral channels for which the simulations were carried out. Channels VIS06, VIS08, and IR016 correspond to the first three spectral bands of the SEVIRI imager, which are generally used to study aerosols [16,20]. Channels VIS04 and IR022 correspond to two additional spectral bands that will be made available by the future imager FCI aboard MTG-I. The spectral responses corresponding to the five channels were used in libRadtran to generate SEVIRI-like and FCI-like values of TOA reflectance. All simulations were performed using a U.S. standard atmosphere 1976 [38].

Table 1. Parameters of Meteosat-Like Values of top-of-atmosphere (TOA) Reflectance Simulated with LibRadtran.

Geometry			Aerosols		Surface	Spectral	
SZA (°) θ_s	VZA (°) θ_v	RAA (°) φ	AOD 550 nm τ	Aerosol type α	Albedo a_s	Channel	Wavelength (µm) λ
0:5:85	0:5:85	0:20:180	0, 0.1, 0.2, 0.3, 0.4, 0.6, 0.8, 1.0, 1.5, 2.0, 3.0	*continental_clean* *continental_average* *continental_polluted* *desert* *maritime_clean* *maritime_polluted*	0:0.05:1	VIS04 [1] VIS06 VIS08 IR016 IR022 [1]	0.44 0.63 0.81 1.64 2.25

[1] Spectral channel of the Flexible Combined Imager (FCI). Other channels correspond to the Spinning Enhanced Visible and InfraRed Imager (SEVIRI).

Table 1 also details the aerosol conditions that were considered for the simulations. The aerosol optical depth (AOD, τ) was supposed to vary from 0 to 3 for a total of six common aerosol types (i.e., *continental_clean*, *continental_average*, *continental_polluted*, *desert*, *maritime_clean*, and *maritime_polluted*). These types are available in libRadtran thanks to the well-known OPAC (optical properties of aerosols and clouds) data base [39] and were chosen to cover most of the aerosol mixtures that are observed by geostationary satellites. Continental types are mostly composed of fine aerosols particles (e.g., sulfates), while the rest of aerosol mixtures correspond to coarser particles (e.g., mineral dust and sea salt). Table 2 details the single scattering albedo (SSA) and the asymmetry parameter (g) for each aerosol type and for channels VIS06 and IR016. Figure 2 shows the phase function that was obtained using the MOPSMAP package (modeled optical properties of ensembles of aerosol particles) [40] for three selected types (i.e., *continental_average*, *desert*, and *maritime_clean*). The phase function is plotted according to the scattering angle (ξ), which is defined as

$$\xi = \pi - \cos^{-1}(\cos\theta_s \cos\theta_v + \sin\theta_s \sin\theta_v \cos\varphi). \quad (1)$$

The predominant forward-scattering peak of aerosols is observed in Figure 2 when scattering angle is close to 0. A secondary scattering peak is also seen in the backward direction when scattering angle is at its maximum. The back-scattering peak of aerosols is stronger for coarse particles such as those included in the types *desert* and *maritime_clean*. Figure 2 also shows the scattering minimum that happens between the two peaks, around 120°.

Table 2. Single scattering albedo and asymmetry parameter for channels VIS06 and IR016 for the six aerosol types considered in this study.

Aerosol type	VIS06		IR016	
	SSA	g	SSA	g
continental_clean	0.94	0.68	0.85	0.68
continental_average	0.89	0.66	0.77	0.66
continental_polluted	0.84	0.65	0.68	0.63
desert	0.92	0.7	0.94	0.69
maritime_clean	0.98	0.75	0.98	0.79
maritime_polluted	0.96	0.74	0.96	0.78

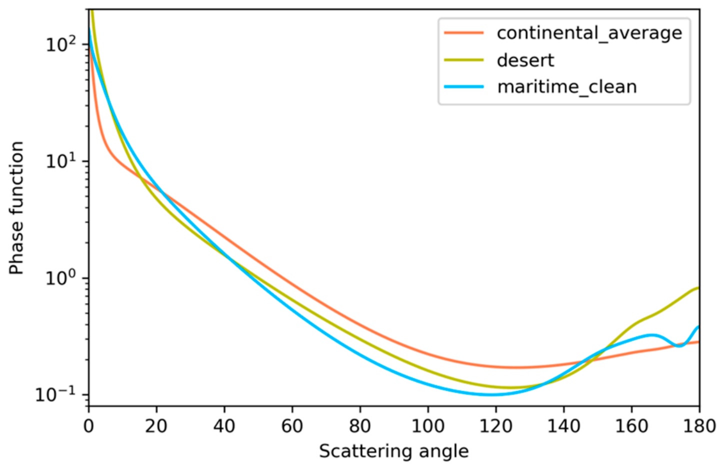

Figure 2. Phase function corresponding to the aerosol types *continental_average*, *desert*, and *maritime_clean* for channel VIS06.

Figure 3 illustrates the radiative transfer simulations that were obtained from libRadtran and the input parameters listed in Table 1. Values of TOA reflectance are shown according to surface albedo for the different values of AOD considered in the LUT. The simulations in the figure correspond to the aerosol type *continental_average* and the geometric configuration set by SZA = 0°, VZA = 30°, and ξ = 150° (see Equation (1) for definition of scattering angle). The different sensitivity to a varying AOD (or, in other words, the aerosol signal) according to the value of surface albedo is observed in Figure 3. On the one hand, an increasing concentration of aerosol particles over a dark surface makes the TOA reflectance increase. On the other hand, the presence of aerosols over brighter surfaces makes the reflectance observed by the satellite decrease. The inflection point happens when the TOA reflectance does not vary with an increasing aerosol load (i.e., surface albedo close to 0.2 in Figure 3). This value corresponds to the critical surface albedo, which is the result of multiple scattering and compensation factors such as surface reflection, aerosol extinction and, to a lesser extent, molecular absorption and Rayleigh scattering.

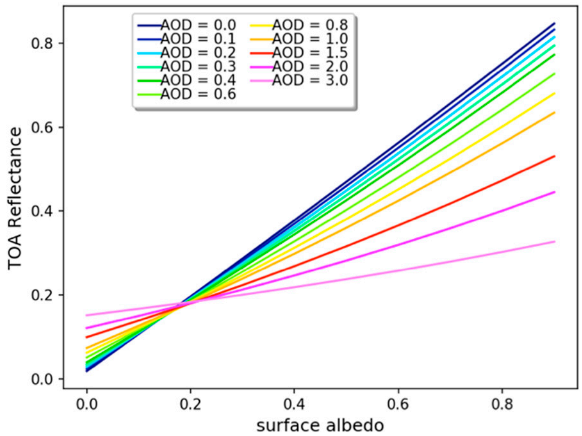

Figure 3. TOA reflectance according to surface albedo for increasing values of aerosol optical depth (AOD). Configuration is set by SZA = 0°, VZA = 30°, ξ = 150°, and channel VIS06.

2.3. Look-Up Table of CSA

The critical surface albedo was calculated for each configuration of geometry, aerosol conditions, and wavelength encompassed by the LUT that is described in the previous section (see bullet 2 in Figure 1). The derivation of CSA was based on the method proposed by Seidel and Popp [32]. A summary of this approach is given here.

As seen in Figure 3, CSA is defined as the value of surface albedo for which a varying AOD (τ) does not alter the satellite measurement at the TOA. Let ρ_γ^{TOA} be the ensemble of TOA reflectance values that are obtained for a given configuration set by θ_s, θ_v, φ, λ, and a given aerosol type α. The value of CSA results in

$$\rho_\gamma^{\text{TOA}}(\tau = \tau_1, a_s = \text{CSA}) - \rho_\gamma^{\text{TOA}}(\tau = \tau_2, a_s = \text{CSA}) = 0, \tag{2}$$

where $\tau_1 \neq \tau_2$.

The calculation of CSA is performed by fitting a fifth-order polynomial to the variation of the TOA reflectance according to AOD

$$\rho_\gamma^{\text{TOA}}(\tau, a_s) \approx \sum_{i=0}^{5} c_i \tau^i, \tag{3}$$

where c_i are the polynomial coefficients, a_s is fixed, and τ is a free variable. The continuity and differentiability of Equation (3) allows the calculation of its partial derivative according to AOD:

$$\frac{\partial \rho_\gamma^{\text{TOA}}(\tau, a_s)}{\partial \tau} \approx \sum_{i=0}^{5} i c_i \tau^{i-1}, \tag{4}$$

from which the CSA can be derived by determining the albedo value that makes Equation (4) equal to zero:

$$\frac{\partial \rho_\gamma^{\mathrm{TOA}}(\tau, a_s = \mathrm{CSA})}{\partial \tau} = 0. \tag{5}$$

The calculation of CSA is illustrated in Figure 4, which shows the derivative of TOA reflectance with respect to AOD for three aerosol types (i.e., *continental_average, desert*, and *maritime_clean*). The three curves correspond to the configuration set by SZA = 40°, VZA = 40°, RAA = 140°, and channel VIS06. The CSA that is derived from each curve corresponds to the value of surface albedo that makes the function equal to 0 (e.g., CSA≈0.22 for *continental_average*). Figure 4 shows the dependency of CSA on aerosol type, which is driven by the different extinction properties.

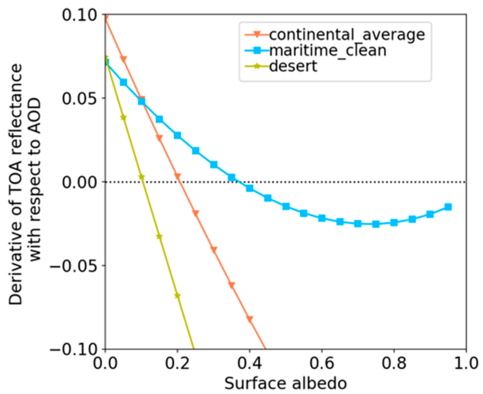

Figure 4. Derivative of TOA reflectance with respect to AOD as a function of surface albedo for AOD = 0.2 and three aerosol types (*continental_average*, *desert*, and *maritime_clean*), when SZA = 40°, VZA = 40°, RAA = 140°, and for channel VIS06.

2.4. Input Data to Compute Maps of dCSA for Meteosat

The LUT of CSA values was exploited to calculate the maps of dCSA corresponding to one complete year of Meteosat observations. The acquisition geometry of the satellite was employed for this purpose. Ancillary information on the commonly observed aerosol properties and surface albedo during the year was also used to calculate the maps of dCSA (see bullet 3 in Figure 1). The period of one year was considered to be enough for this study, as it allowed the consideration of all the major changes in geometry and properties of surface and aerosols related to geostationary satellites.

2.4.1. Geometry

The angles describing the acquisition geometry (SZA, VZA, and RAA) of Meteosat observations were directly obtained from SEVIRI ancillary data. The three angles were available at the SEVIRI acquisition frequency of 15 minutes during the year 2012. The geometry of the future FCI imager (corresponding to channels VIS04 and NIR22 in this study) was assumed to be the same as SEVIRI's since MTG-I will be situated at the same position than MSG. The increase of the temporal and spatial resolution of FCI versus SEVIRI was not taken into account in this study for the sake of simplicity.

2.4.2. Aerosol Properties

Information on aerosol content and type were obtained from the Copernicus Atmospheric Monitoring Service (CAMS, https://atmosphere.copernicus.eu). Monthly averages were calculated from CAMS reanalysis for the AOD of each of the five aerosol components that are considered in the CAMS system, namely sulfates (SU), dust (DU), sea salt (SS), black carbon (BC), and organic matter (OM). The total AOD was calculated as the sum of the five AOD values. Monthly estimates of the predominant aerosol type were also obtained from CAMS data. The methodology in [41] was followed to determine the OPAC aerosol type that corresponds to a given set of CAMS individual AOD values.

For example, this approach chooses the OPAC *desert* aerosol type when the AOD of the DU component is higher than 40% of the total AOD. OPAC aerosol types *Antarctic* and *artic* were not considered in our study since polar regions are not observed from the geostationary orbit. Similarly, the OPAC type *urban* was excluded since it is rarely observed at the spatial resolution of Meteosat (i.e., ~5 km over Europe). The absence in the OPAC data base of an aerosol mixture related to biomass burning particles resulted in the choice of the type *continental_polluted* (i.e., the one with the highest content of black carbon) for regions where these carbonaceous particles predominate.

2.4.3. Surface Albedo

Monthly averages of surface albedo were derived from two sources. First, land surface albedo was taken from the reanalyzed MSG daily surface albedo (MDAL) product of the Satellite Application Facility for Land Surface Analysis (LSA SAF) program of EUMETSAT (http://lsa-saf.eumetsat.int/). This satellite product provides the land surface albedo estimated from the MSG/SEVIRI platform thanks to the inversion of a radiative transfer-based model [42]. The accuracy of this product has proved to be in agreement with other satellite products and ground measurements [43]. The values of surface albedo for the future FCI channels VIS04 and IR022 were calculated based on the albedos for the SEVIRI channels VIS06, VIS08, and IR016 using a linear regression approach. Regression coefficients were derived from a data base of thousands of spectral signatures of natural surfaces, as it was done by Samain et al. in [44] to convert TOA radiances from one satellite to another. Second, static values were chosen to describe ocean surface albedo for the five spectral channels considered in this study (see Table 3). The chosen values correspond to the average albedo of sea water for a non-glint condition [45].

Table 3. Surface albedo for water surfaces.

Channel	Surface Albedo
VIS04	0.1
VIS06	0.05
VIS08	0.01
IR016	0
IR022	0

2.5. Calculation of Maps of dCSA for Meteosat

The maps of dCSA for Meteosat were calculated based on the LUT of CSA and the inputs described in the previous sections (see bullet 4 in Figure 1). The dCSA for each pixel of a given Meteosat image was calculated by doing

$$\mathrm{dCSA}(x,y,t,\lambda) = \mathrm{CSA}\Big(\theta_s^{x,y,t},\ \theta_v^{x,y,t}, \varphi^{x,y,t}, \tau^{x,y,t}, \alpha^{x,y,t}, \lambda\Big) - a_s^{x,y,t,\lambda}, \tag{6}$$

where $a_s^{x,y,t,\lambda}$ corresponds to the surface albedo described in Section 2.4.3 for coordinates $\langle x,y\rangle$, instant of time t, and channel with central wavelength λ. Equation (5) was applied after the linear interpolation of the LUT of CSA in order to provide the exact CSA value corresponding to the geometry $\langle\theta_s^{x,y,t},\ \theta_v^{x,y,t}, \varphi^{x,y,t}\rangle$ and the aerosol load $\langle\tau^{x,y,t}\rangle$. Aerosol type ($\alpha$) was not interpolated.

The operation in Equation (5) was made every hour for one year of Meteosat observations. This temporal resolution is only slightly superior to the temporal resolution of Meteosat platforms, with 15 minutes for the current imager SEVIRI and 10 minutes for the future imager FCI. A series of 8760 maps (i.e., 24 hours per 365 days) of dCSA were obtained for the Earth disk that is observed by Meteosat. The variation of the information contained in one year of Meteosat observations (both spatially and temporally) comes from the instantaneous geometry, the monthly aerosol properties, and the monthly surface albedo described in Section 2.4. A temporal interpolation was done for AOD and surface albedo to avoid jumps at the beginning of each month. In particular, a linear interpolation was performed considering that the monthly averages correspond to the fifteenth day of the month. Aerosol type was not interpolated in time.

The absolute value of Equation (5) is often used in the results section. The reason is that the sensitivity to the aerosol signal is independent of the sign of dCSA. The only difference is that a positive (respectively, negative) dCSA means that aerosols appear brighter (respectively, darker) than the underlying surface.

3. Results

This section presents the results that were obtained following the methods described in Section 2. First, Section 3.1. investigates the dependency of CSA on the different parameters of the generated LUT. Second, the calculation of a map of dCSA for one Meteosat image is illustrated in Section 3.2. The results section continues with the analysis of the one year of maps of dCSA for Meteosat. The analysis was done according to the different scales of time that are made possible by geostationary satellites, namely diurnal (Section 3.3), seasonal (Section 3.4), and yearly (Section 3.5). Each temporal scale is related to particular variations in aerosol properties and solar geometry. This investigation was also carried out over the spatial domain by inspecting the values of dCSA across the regions of the Earth encompassed by the Meteosat disk. Each region is related to different viewing angles. Channel VIS06 from SEVIRI was considered for most of the experiments due to its proximity to the traditional wavelength used in aerosol remote sensing, namely 550 nm.

3.1. Dependence of CSA on the Remote Sensing Parameters

The LUT of CSA values obtained in Section 2.3 depends on solar and viewing geometry ($\theta_s, \theta_v, \varphi$), wavelength ($\lambda$), and aerosol properties. Figure 5 illustrates these dependences by showing the variation of CSA according to joint solar–view zenith angle (JZA), scattering angle, AOD, and aerosol type. JZA is defined as the sum of VZA and SZA [46] and is linked to the air mass. For geostationary satellites, high SZA happens in the local morning and evening and high VZA is related to the regions located along the outer edge of the Earth's disk. Second order polynomials were fitted to the CSA points in Figure 5a–c in order to highlight the main trends. A box plot is used for Figure 5d to study the correlation between CSA and aerosol type.

The increase of the CSA with JZA that is observed in Figure 5a comes from two reasons. First, the higher scattering of aerosols in the forward direction, which is sensed from space when zenith angles are high, requires a higher value of albedo to reach the CSA situation. Second, the increase of the air mass with JZA results in a higher atmospheric scattering, which also makes the CSA increase. The increase of CSA for low JZA is due to the back-scattering peak of some aerosol types (e.g., *maritime_clean*). The spread in Figure 5a is due to the variations in scattering angle. Figure 5b underlines the correlation of CSA with the aerosol phase function by showing the maximum values of CSA for low and high scattering angles (close to the forward and backward peak, respectively). Analogously, the lowest values of CSA are obtained when the phase function is at its lowest (i.e., $\xi \approx 100°–140°$, see Figure 2). The spread of CSA values comes from the varying sun/view zenith angles (and; therefore, air mass) for a given scattering angle. Figure 5c shows a strong independence of CSA with AOD. The slight increase of CSA with AOD is illustrated in Figure 3, which shows that the curves of TOA reflectance do not cross exactly in the same point. Finally, Figure 5d shows the relation between CSA and aerosol type. The aerosol types that were considered in our study were sorted according to their SSA for channel VIS06 in ascending order (see Table 2). A positive correlation is observed between CSA and SSA, making CSA greater for aerosol types with high scattering properties. Again, the presence of a back-scattering peak for maritime and *desert* aerosol types results in higher values of CSA. The spread of CSA values in Figure 5c,d comes from the variations in acquisition geometry.

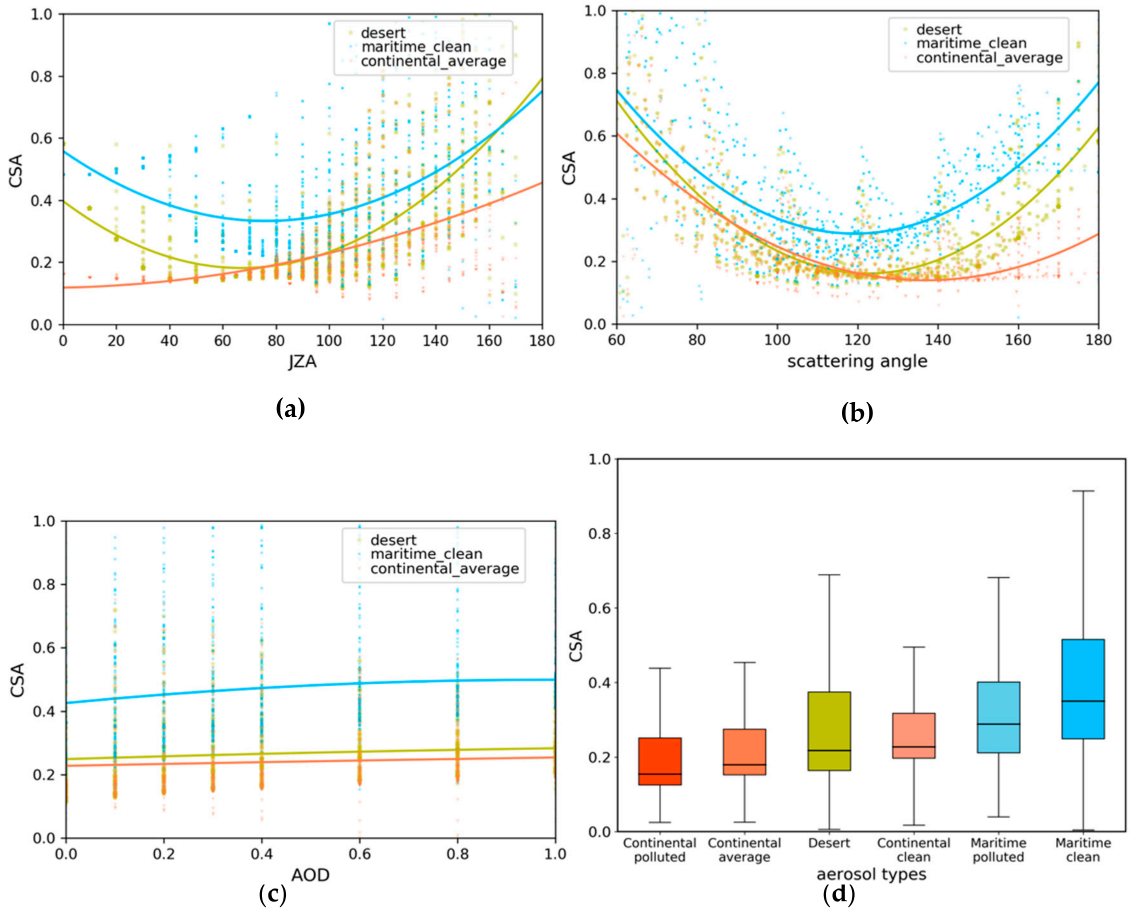

Figure 5. Sensitivity study of the critical surface albedo (CSA) for three aerosol types (*continental_average*, *desert*, and *maritime_clean*) and for channel VIS06 against different variables: (**a**) CSA versus JZA when AOD = 0.2, (**b**) CSA versus scattering angle when AOD = 0.2, and (**c**) CSA versus AOD when VZA = 40°. The box plot in (**d**) shows CSA versus aerosol type when AOD = 0.2. The box extends from the first to third quartile values of the data, with a line at the median. The whiskers extend from the box to show the fifth and ninety-fifth percentiles.

3.2. Calculation of the Map of dCSA for One Meteosat Image

Figures 6 and 7 summarize the calculation of the dCSA for the Meteosat image corresponding to 21 June 2012 at 12:00 UTC. Channel VIS06 from SEVIRI was considered for this experiment. Figure 6 shows the inputs used to calculate the dCSA map for the selected Meteosat image. Figure 7 shows the maps of CSA and dCSA that were obtained by following the proposed approach. In this experiment, the absolute values of dCSA are considered. A logarithmic color scale is used in Figure 7 to enhance the low values of dCSA, which are associated with the lower aerosol sensitivity. As it can be seen in Figure 7a, CSA is driven by aerosol type and acquisition geometry. Higher values of CSA are obtained for highly scattering aerosol particles (e.g., maritime types) and along the outer edge of the Meteosat disk, where high values of JZA (and; therefore, lower scattering angles) are found (see Figure 6b,d, respectively). Figure 7b also shows the impact of aerosol type and geometry on the map of dCSA. Furthermore, dCSA is shaped by the spatial distribution of surface albedo (see Figure 6a) or, more precisely, the relation between the surface albedo and the scattering power of aerosols. For example, the highly scattering maritime aerosols result in high values of dCSA over the dark ocean surfaces. The highest values of dCSA are found along the outer edge of the Meteosat disk due to the high VZA. Over land; however, the higher albedo values and the presence of less scattering aerosols (e.g., *desert* and continental types) result in lower dCSA values. Another reason is the generally weaker aerosol brightness due to the low scattering angles happening at 12:00 UTC (see Figures 2 and 6e), when the Sun is behind Meteosat. As expected, no strong relation is observed between AOD and dCSA due to the weak dependence between these two variables.

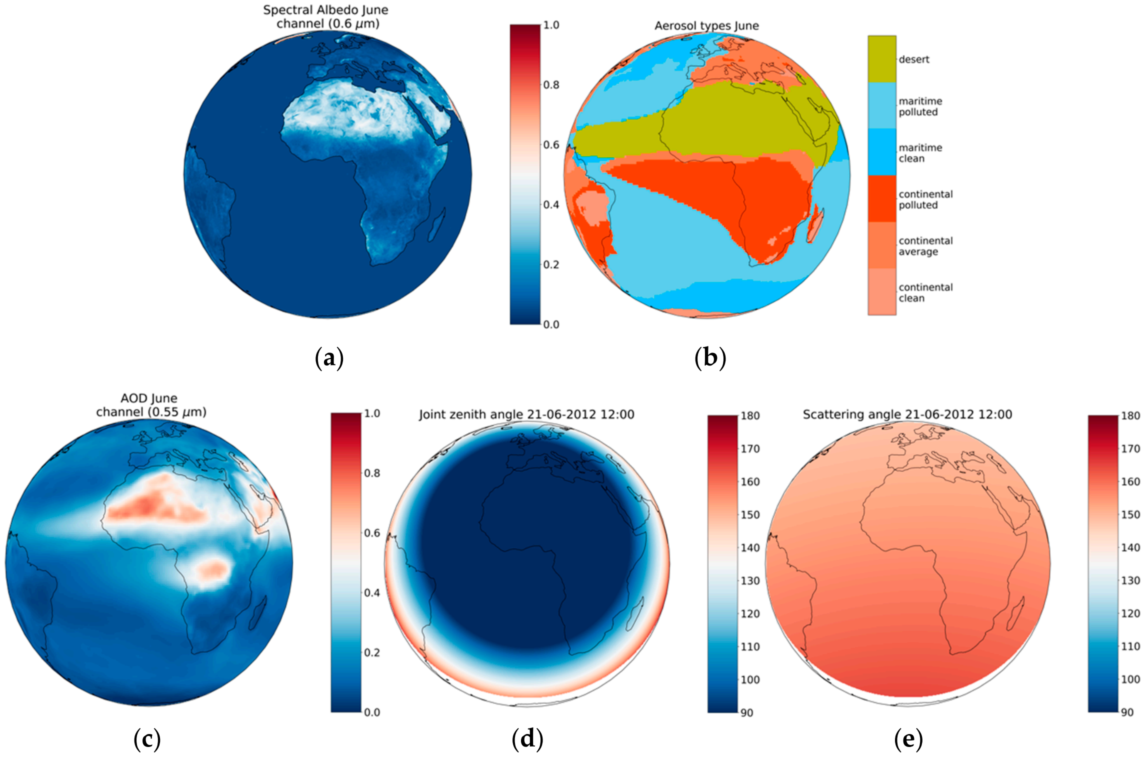

Figure 6. Inputs used to calculate dCSA for 21 June 2012 at 12:00 UTC: (**a**) Average surface albedo for June and VIS06 channel, (**b**) predominant aerosol type for June, (**c**) average AOD at 550 nm for June, (**d**) joint solar–view zenith angle in degrees for the given Meteosat image, and (**e**) scattering angle in degrees for the given Meteosat image.

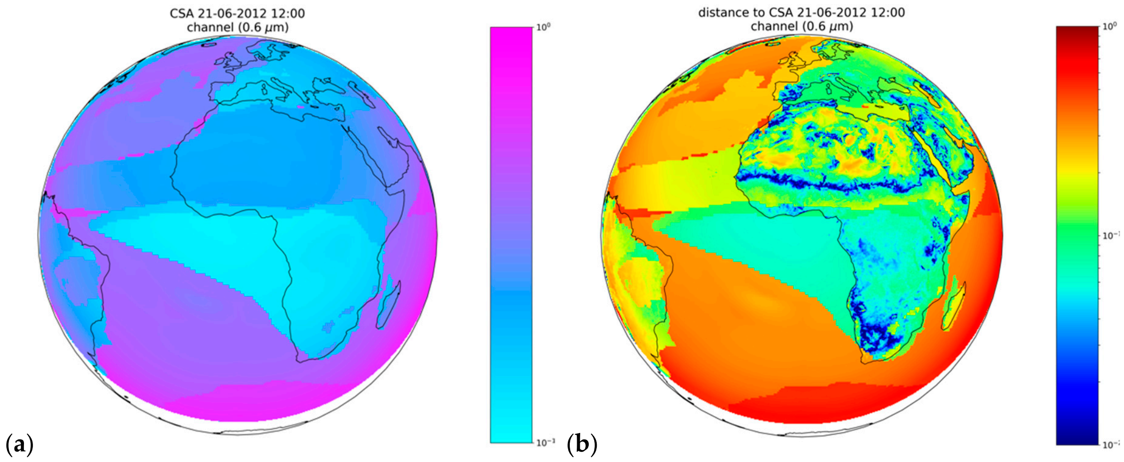

Figure 7. Results for 21 June 2012 at 12:00 UTC with (**a**) CSA and (**b**) dCSA for the given Meteosat image.

3.3. Diurnal Study

This experiment investigates the diurnal variation of dCSA, which is often strong due to the evolution of solar geometry during the day. These sub-daily variations are sensed by geostationary imagers thanks to their high temporal resolution. This study was conducted over several locations in order to investigate the dependence of the diurnal variation across the geostationary disk.

The location of seven ground stations belonging to the Aerosol Robotic Network (AERONET) were considered in this study. Figure 8 situates these stations with yellow circles and the sub-satellite point with a red circle. Ground stations were selected to cover varied geometric configurations and aerosol activity. The station Black_Forest_AMF is situated in a needle-leaved forest in Western Germany, where continental aerosols predominate throughout the year [47]. Station Ilorin is located in a shrubland area in Nigeria that is often impacted by Saharan dust in spring and biomass burning aerosols the rest of the year. Agoufou is situated in a grassland area in Northern Mali, which can be heavily impacted by dust storms [48]. Desert aerosols are also common in the station Solar_Village, which is located in a bare area northwest of Riyadh in Saudi Arabia. Station Rome_Tor_Vergata is located in the suburbs of Rome close to the Mediterranean Sea, which may bring maritime aerosols in the wintertime. Finally, two stations are selected to encompass biomass burning aerosols in two different regions of the world. First, Gorongosa is situated in a broad-leaved forest in Mozambique, where grass fires are common in the second half of the year [49]. Second, Alta_Floresta is located in a forest area in Brazil, south of the Amazon forest, where fires may occur until November.

Figure 8. Yellow circles pinpointing the location of the seven ground stations considered for the inspection of the diurnal variation of dCSA. Red circle shows the sub-satellite point for Meteosat.

Figure 9 shows the monthly averaged diurnal evolution of dCSA for the seven locations and for selected months. This information was obtained by averaging, for each month, the dCSA values corresponding to the location of the selected AERONET stations. These data were extracted from the full year of maps of dCSA that was generated following the approach in Section 2.5. Again, channel VIS06 from the SEVIRI imager was considered in this study. Red vertical bars correspond to the standard deviation of the hourly values over the month. Horizontal axis corresponds to time in units of UTC hour. The left vertical axis corresponds to the dCSA value from –1 to 1. A double logarithmic scale was chosen to enhance the values of dCSA close to zero and; therefore, related to a low sensitivity to aerosols. Very low values of dCSA were shaded in red color to highlight the interval where sensitivity becomes critically low. The right vertical axis in gray color corresponds to the monthly averaged diurnal variation of the scattering angle, which is shown by a gray dashed line. Finally, the average surface albedo and the predominant aerosol type are, respectively, given in the left-bottom and right-bottom corners of the plots in Figure 9.

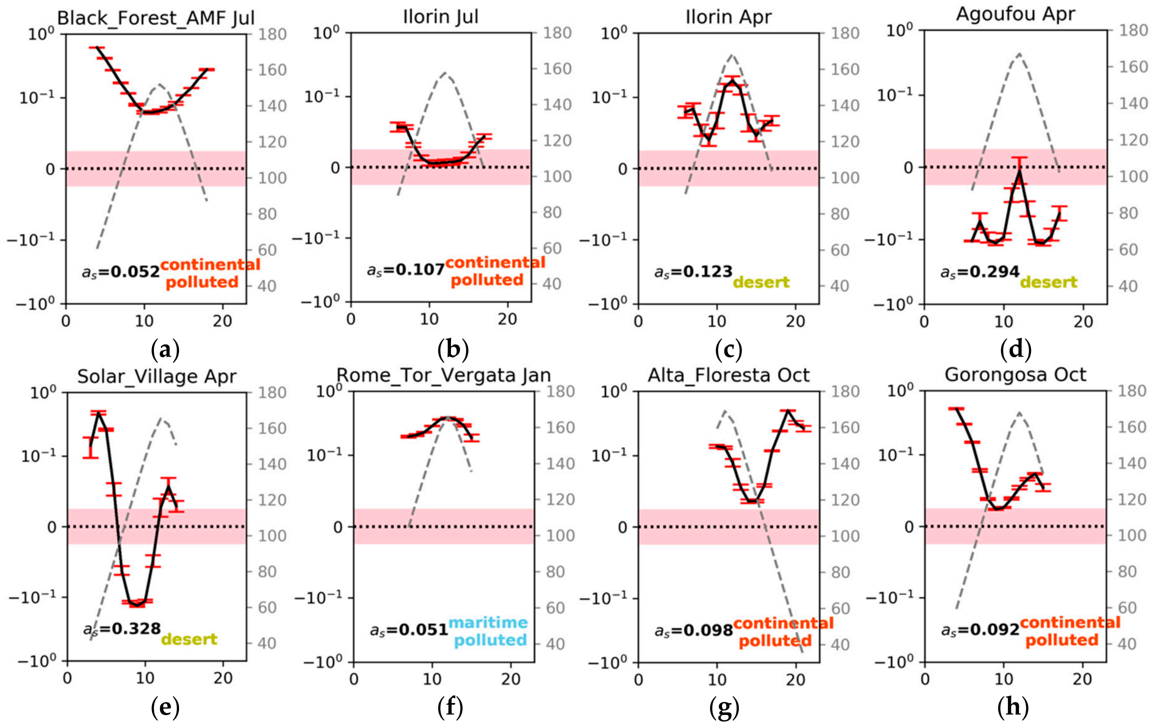

Figure 9. Monthly averaged diurnal variation of dCSA for (**a**) Black_Forest_AMF in July, (**b**) Ilorin in July, (**c**) Ilorin in April, (**d**) Agoufou in April, (**e**) Solar_Village in April, (**f**) Rome_Tor_Vergata in January, (**g**) Alta_Floresta in October, and (**h**) Gorongosa in October. Horizontal axes correspond to time in hour UTC. Left vertical axes correspond to dCSA, which is shown by a black curve. Red vertical bars correspond to the monthly standard deviation of each hourly value of dCSA. Right vertical axes correspond to scattering angle in degrees, which is shown by a gray dashed line. The predominant aerosol type and average surface albedo are given for every plot.

Figure 9a shows the diurnal variation of dCSA for station Black_Forest_AMF in July. The presence of continental aerosols over the predominant dark vegetation resulted in positive values of dCSA during the day. The large variation during the day of the scattering angle resulted in a strong diurnal variation of dCSA, with maxima in the morning and in the evening when scattering angle is low and scattering is high (see Figure 2). The variation of geometry comes from the solar zenith angle, which varies greatly during the day in the European summer. A similar correlation between dCSA and solar zenith angle is observed in Figure 9b corresponding to the station Ilorin in July. In this case, dCSA decreased down to values close to zero. The reason to this lower sensitivity is the higher surface albedo and the lower excursion of the scattering angle during the day due to the proximity of this station to the sub-satellite point (see Figure 8). The U-shaped diurnal cycle of dCSA that is observed in Figure 9a,b is typical of stations with continental aerosols with a weak back-scattering peak (see Figure 2). Figure 9c shows a different diurnal shape for Ilorin in April, when dust aerosol particles are predominant. The sensing of the stronger back-scattering peak of the *desert* aerosol type (see Figure 2) resulted in a maximum of sensitivity at midday. The higher SSA of dust aerosols with respect to continental aerosols (see Table 2) explains the higher values of dCSA for Ilorin in April with respect to July. The impact of surface albedo on dCSA is illustrated in Figure 9d, which shows the diurnal cycle for the same month of April in Agoufou. Despite the similar geometry and aerosol type compared to Ilorin, the higher albedo of Agoufou (0.294 versus 0.123) made the dCSA lower on average while the same diurnal shape prevailed. In this case, the aerosols are darker than the surface, which gave negative values of dCSA. Figure 9e shows the diurnal cycle for Solar_Village in April, which is also covered by dust particles but it is related to lower scattering angles due to the greater distance to the sub-satellite point. While maxima of dCSA are again observed in the morning and evening, a strong minimum is observed around noon. This comes from the sensing of the lowest scattering values of the phase function (see Figure 2). It is interesting to note that, for this station, aerosols are brighter than the surface in the morning and evening (positive dCSA values) but they are darker at noon (negative dCSA values). Figure 9f details the diurnal cycle of dCSA over Rome_Tor_Vergata during January. The presence of highly scattering maritime aerosols over a rather dark surface resulted in high values of dCSA during the day. The occurrence of high scattering angles due to the lower sun in the European winter also contributed to this high sensitivity, which resulted in a maximum of dCSA at midday when the back-scattering peak of maritime aerosols is sensed (see Figure 2). Finally, the presence of biomass burning aerosols (represented by the *continental_polluted* type) is investigated in Figure 9g,h corresponding to stations Alta_Floresta and Gorongosa, respectively. The variation of dCSA during the day in these two cases is similar but symmetrical with respect to the vertical axis defined by the local noon. Indeed, the two stations are located southeast and southwest of the sub-satellite point, which give rather symmetrical scattering angles during the day. The lowest values of dCSA were similarly obtained around the local noon for the two stations when the phase function reaches its minimum.

3.4. Seasonal Study

This experiment explores the variation of dCSA during the four seasons of the year. The Earth's axial tilt relative to the ecliptic plane results in the motion of the Sun between the tropics of Cancer and Capricorn. This variation of the solar position across the seasons has an impact to the value of dCSA. Another impact comes from the variations of aerosol properties with seasons. This experiment was conducted by inspecting the maps of dCSA corresponding to the four meteorological seasons (i.e., winter for DJF, spring for MAM, summer for JJA, and fall for SON). Seasonal maps were obtained by averaging the dCSA obtained for all Meteosat images corresponding to each season.

Figure 10a shows the seasonal maps of absolute dCSA obtained over the Meteosat disk for channel VIS06. The seasonal averages of the inputs used are given in Figure 10b–f. As it was seen in Figure 7b, dCSA is strongly dependent on geometry, aerosol type, and surface albedo. The variation with time of these parameters drive the seasonal evolution of dCSA for the different regions of the disk. For example, Western Europe shows rather high values of dCSA during the most part of the year due to the predominance of scattering maritime aerosols according to CAMS [50]. The less scattering continental aerosols happening in the summer reduce the contrast with the surface, thus giving lower values of dCSA. Results on Northern Africa show a dependence on the value of surface albedo with, for example, the sandy deserts of El Djouf (between Mauritania and Mali) and Ténéré (in Niger and Chad) obtaining the highest values of dCSA due to their high surface albedo [51]. On the contrary, the Sahel region shows the lowest values of dCSA due to its medium value of albedo, which results in a strong coupling with the predominant *desert* aerosol type during the year [50]. The coast of Ghana and Ivory Coast also obtained low values of dCSA due to the low albedo and the predominant *continental_polluted* aerosols found in this region. The value of dCSA do not change much across the seasons in this region due to its proximity to the sub-satellite point resulting in a low variation of solar geometry. The only exception happens in spring, when the arrival of dust particles from the Sahara Desert result in a higher contrast between the aerosols and the surface. The impact of the varying geometry across the seasons is more visible in Namibia and Western South Africa where *continental_polluted* aerosols predominate during the year. The sensitivity to aerosols in this region is driven by the geometry, with a minimum in summer, when the scattering angle is at its highest (and thus the phase function reaches its minimum), and a maximum in winter, when the scattering angle is at its lowest (and thus the phase function reaches its maximum). Similar to the brightest regions in the Sahara Desert, the sand dunes in the Namib Desert show high values of dCSA throughout the year due to the contrast between the surface albedo of this region and the overlaying aerosols. Over ocean, dCSA is high in general due to the presence of maritime aerosols. Lower values happen over the Gulf of Guinea where darker *continental_polluted* aerosols were considered due to the presence of biomass burning in this area [52].

The absence of a strong back-scattering peak for this type of particles combines with the high scattering angles happening for regions near the sub-satellite point.

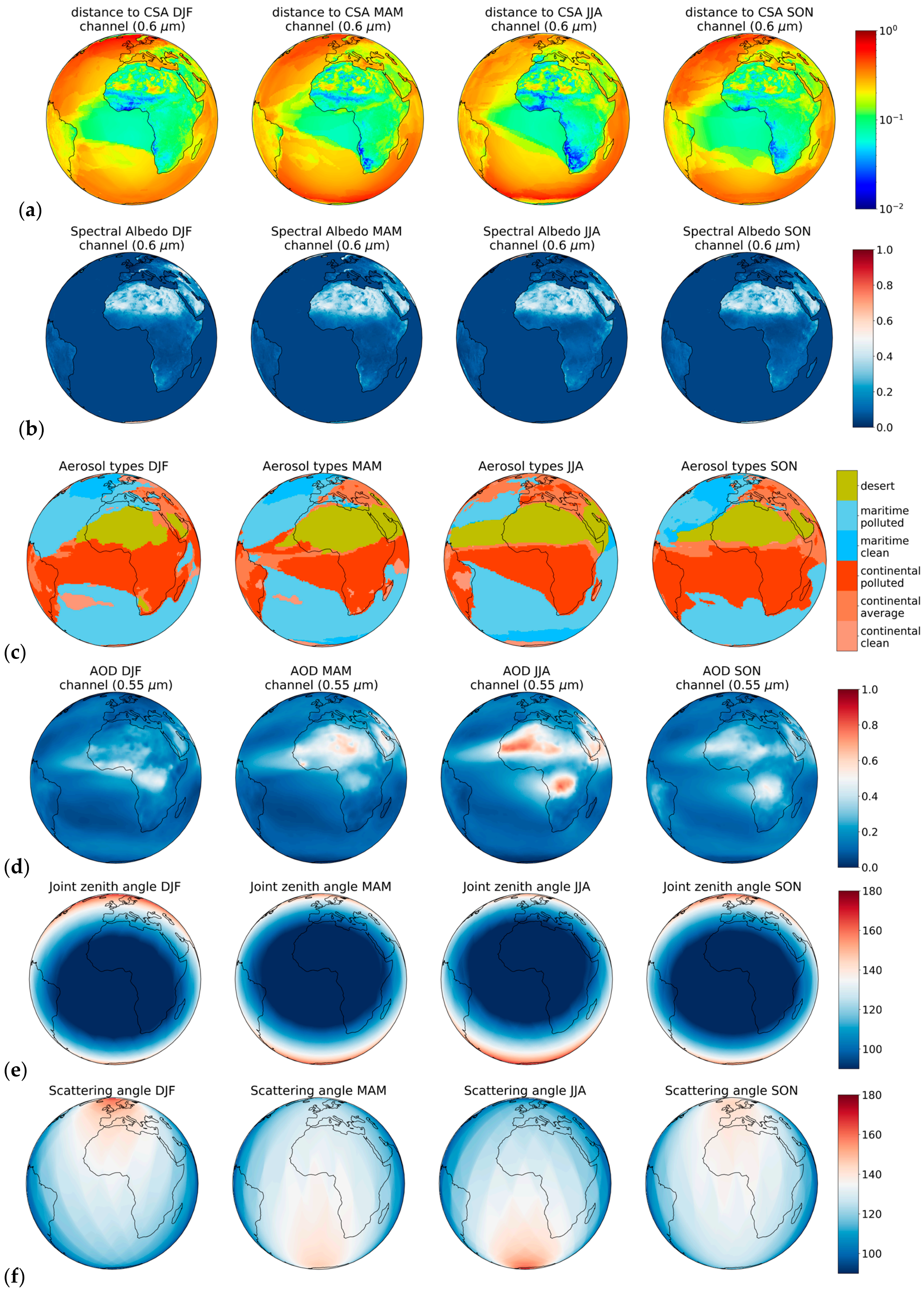

Figure 10. Seasonal maps of (**a**) dCSA for VIS06, (**b**) surface albedo for VIS06, (**c**) predominant aerosol type, (**d**) AOD at 550 nm, (**e**) JZA in degrees, and (**f**) scattering angle in degrees. Seasons are ordered by columns.

3.5. Yearly Study

The last experiment investigates dCSA across the Meteosat disk averaged over the year. This experiment conducted on channel VIS06 is intended to evaluate the average sensitivity of Meteosat platforms to aerosol particles.

Figure 11a shows the yearly map of absolute dCSA obtained over the Meteosat disk for channel VIS06. The yearly averaged inputs are given in Figure 11b–f. As it can be seen, the map of dCSA is similar to the seasonal maps obtained in the previous experiment (see Section 3.4). The highest values of dCSA are obtained for the outer edge of Meteosat, over ocean, and for very bright desert regions. In contrast, low values of dCSA happen across the Sahel, and the coast of Namibia and Ivory Coast. In general, dark surfaces are related to higher values of dCSA, especially if they are far away from the sub-satellite point (e.g., South America). Again, an impact of the aerosol load on the dCSA map is not observed (see Figure 11d).

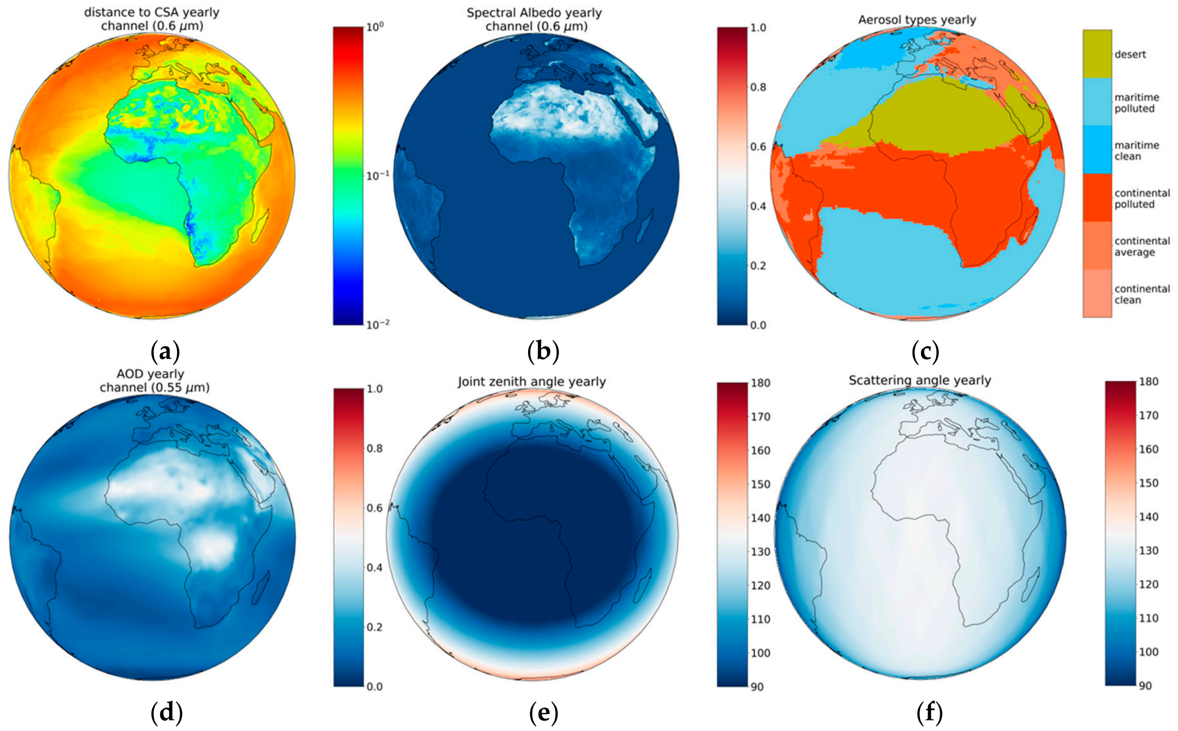

Figure 11. Maps of yearly dCSA for VIS06 and yearly averaged inputs: (**a**) dCSA, (**b**) surface albedo, (**c**) predominant aerosol type, (**d**) average AOD at 550 nm, (**e**) joint solar–view zenith angle in degrees, and (**f**) scattering angle in degrees.

3.5.1. Wavelength Dependence

The yearly experiment continues with the investigation of the impact of the sensing wavelength on dCSA. Figure 12 summarizes the yearly averaged maps of absolute dCSA (in the upper row) and the corresponding surface albedo (in the lower row) that were obtained for the five channels from imagers SEVIRI and FCI (i.e., VIS04, VIS06, VIS08, IR016, and IR022, see Table 1). The inputs used in this experiment are given in Figure 11b–f.

As it can be seen in Figure 12(top), the maps of dCSA show significant variations for the different channels. These changes result from the spectral variation of aerosol properties and surface albedo. On the one hand, dCSA is higher for greater wavelengths due to the generally lower reflectivity of fine aerosols (see Table 2). On the other hand, dCSA is driven by the spectral signature of the land surfaces. For example, the dCSA for arid regions, such as the Sahara Desert, increases with wavelength, reaching its maximum for channel IR016, similarly to the albedo of bare soil, as it is shown by Figure 12(bottom). In this case, the surface is brighter than aerosols for all wavelengths. In contrast, vegetated areas obtain higher values of dCSA for wavelengths for which they appear darker, as overlaying aerosols are usually brighter. This is the case of the Amazon Forest, which obtains the highest value of dCSA for channel VIS04. Regions with intermediate surface albedo, such as the Sahel, show higher values of dCSA for longer wavelengths (i.e., channels IR016 and IR022). This increase comes from the increasing spectral signature of bare soils combined with the flat signature of the predominant coarse dust particles (see spectral variation of SSA in Table 2). It is also worth mentioning the increase of dCSA with wavelength for Namibia and Western South Africa. The reason in this case is not only the increase of surface albedo with wavelength, but also the decrease of aerosol scattering with wavelength. Regarding ocean surfaces, variations of dCSA are in agreement with the decreasing spectral signature of water, as it is shown by Figure 12(bottom). Values of dCSA reach are minimum for channel VIS04, when water reflectance is highest becoming close to that of *continental_polluted* aerosols (e.g., in the Gulf of Guinea). Values of dCSA increase with wavelength, reaching its maximum for channel VIS08. However, it decays again with wavelength due to the decrease of the reflectance of fine aerosol particles for channels IR016 and IR022 (see Table 2).

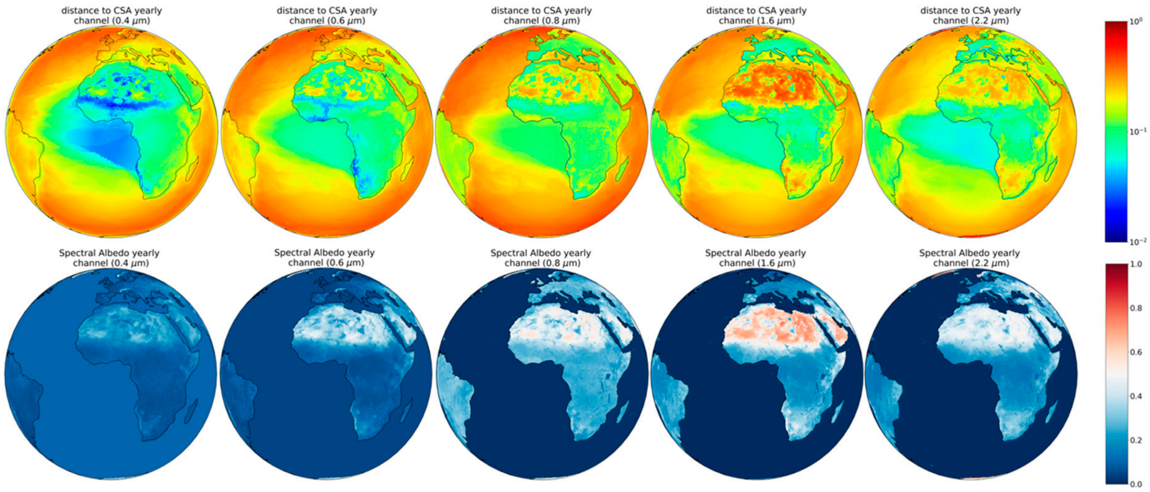

Figure 12. Study on the impact of wavelength on dCSA with (top row) maps of yearly dCSA and (bottom row) the corresponding surface albedo. Columns correspond to channels in this order, VIS04, VIS06, VIS08, IR016, and IR022. Inputs are shown in Figure 11b–f)

3.5.2. Impact of Cloudiness

The yearly experiment concludes with the study of the impact of cloudiness on the yearly averages of dCSA. The fact that most aerosol retrieval methods using passive remote sensing data do not work in the presence of clouds [3] is taken into account in this experiment. The yearly average of dCSA for channel VIS06 was calculated a second time considering only the dCSA values corresponding to cloud-free observations of Meteosat during the year. This is done to provide a more accurate idea of the potential of spaceborne passive observations for aerosol retrieval. Information on cloudiness was taken from the cloud mask product from the Satellite Application Facility on Support to Nowcasting and Very Short Range Forecasting (NWC SAF) program (http://www.nwcsaf.org/) derived from SEVIRI observations [53].

Figure 13(left) shows the occurrences of cloud-free Meteosat images during the year as it is derived from the NWC SAF product. Figure 13(right) shows the yearly average of the difference between values of dCSA calculated for all-sky Meteosat pixels (i.e., cloud-free and cloudy conditions) and values of dCSA calculated only for clear-sky Meteosat pixels. The resulting map shows in blue(red) the regions that obtained a lower(higher) value of dCSA when only cloud-free conditions were considered.

As expected, the changes in the yearly dCSA appear only for regions that are covered by clouds at some point of the year. Eastern and Northern Europe increase the average dCSA thanks to the filtering of many observations corresponding to winter, when cloudiness is higher and dCSA is lower (see Figure 10a). The same thing happens along the coast of Kenya and Tanzania, which shows an increase of the sensitivity to aerosols due to the link of the cloudy observations to the lowest values of dCSA. On the other hand, the yearly average of dCSA drops for many regions across the outer disk of Meteosat including a part of the Amazon Forest and the Mediterranean Sea. For the latter region, the reason comes from the filtering of the cloudy pixels during winter corresponding to a high dCSA due to the predominance of maritime aerosols. In the drier (and; therefore, clearer) summer, the presence of the less scattering continental particles results in lower values of dCSA.

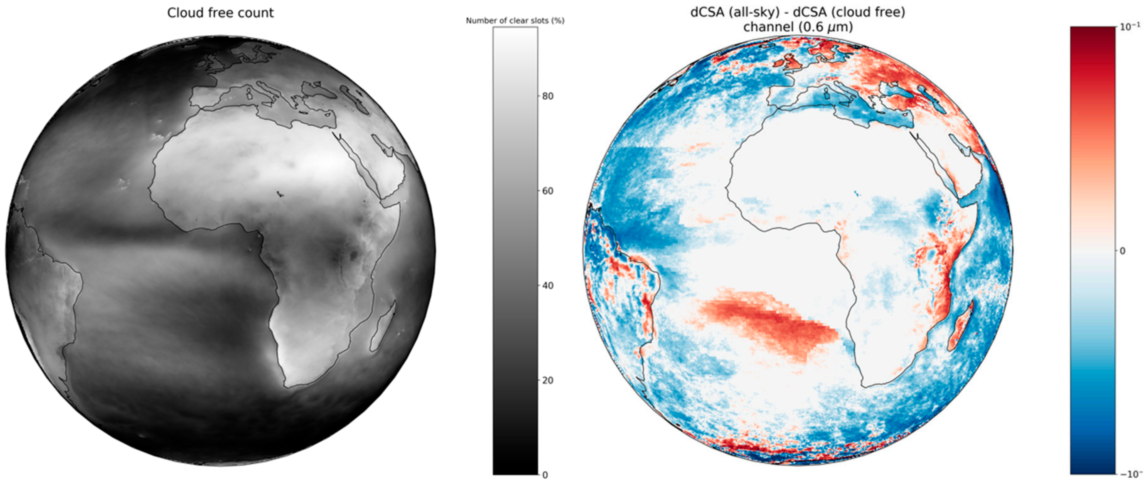

Figure 13. Maps of (**a**) cloud-free occurrence in percentage and (**b**) differences in dCSA due to consideration of cloud-free pixels only.

4. Discussion

4.1. dCSA and Sensitivity to Aerosols

The results reported in the previous section provide a global view of the potential of geostationary platforms, and Meteosat in particular, for aerosol remote sensing. This potential is evaluated by means of the difference between the albedo of the observed surface and the corresponding CSA. The basis of this study is the link between the difference between the observed surface albedo and the corresponding CSA (i.e., dCSA) and the sensitivity of remote sensing observations to a varying aerosol concentration (see Figure 3). The greater the value of dCSA, the higher the sensitivity to the AOD and the potential to retrieve it.

Overall, aerosol remote sensing is generally possible due to the positive values of dCSA. This comes from the generally higher brightness of the aerosol signal with respect to the surface signal at the TOA level [27]. In this context, dark surfaces (e.g., dense forests) and bright aerosols (e.g., sea salt particles) correspond to the most suitable conditions for AOD retrieval. Nonetheless, aerosol retrieval becomes more challenging for some regions on Earth, especially over land, due to the proximity of the surface albedo to CSA. Even in these situations, geostationary satellites have the potential to retrieve the AOD thanks to the large variety of geometric information that they make available.

4.1.1. Geometric and Temporal Information

The variation of geometry in geostationary observations is mainly driven by the changing illumination by the Sun during the day, which is sensed thanks to the high temporal resolution of the imagers. This large diurnal variation of geometry can make aerosol retrieval possible at some instants of time despite the impossibility for the rest of the day. The diurnal variation of the scattering angle always follows a concave function with a maximum at the local noon (12:00 UTC for Meteosat due to its position at 0° of longitude, see Figure 9). Different parts of the phase function of aerosols are; therefore, sampled during the day. For example, the sensing of the shoulder of the forward peak in the local morning and the local evening results in a maximum of sensitivity to aerosols at these times. In contrast, the minimum of the phase function is usually sensed at the local noon when scattering angle is high. At this time, the reduced aerosol brightness becomes similar to that of the surface. An exception happens for regions close to the sub-satellite point where scattering angles become close to 180°. In this situation, the back-scattering peak of some types of aerosols is sensed, making the aerosol signal stronger again.

The variations of solar geometry with seasons may also increase the potential of geostationary observations. This is the case of periods of time showing large variations of geometry during the day (e.g., summer in Northern hemisphere). Seasons may also bring changes in cloudiness and aerosol type, which may also impact the sensing of aerosols. This is the case of the increased sensitivity over Europe in winter due to the predominance of maritime aerosols and the reduced sensitivity over the Amazon Forest due to persistent cloudiness during favorable retrieval situations (see Section 3.5.2).

4.1.2. Spatial Information

The sensitivity to AOD also depends on the region of study due to the different geometry. For example, the higher view zenith angles corresponding to the outer edge of the geostationary disk make aerosols appear brighter due to their forward-scattering peak. It is worth mentioning that the enhanced sensitivity to AOD that is observed in this region may be impacted as one goes to the limb by the loss of spatial resolution and the viewing of more air mass. The results reported in Section 3 show significant differences between land and ocean. First, continental surfaces are generally closer to CSA because they are mostly located in the central regions of the Meteosat disk (e.g., Africa), which correspond to lower zenith angles. Furthermore, albedo of land surfaces is often closer to the reflectivity of aerosols, in part because of the similar chemical composition of some aerosols and surfaces (e.g., dust aerosols over dusty areas) [27]. Some of these regions (e.g., the Sahel) neither appear brighter nor darker than aerosols, making them difficult for aerosol remote sensing. On the other hand, significantly dark or bright surfaces usually result in a sufficient contrast that makes AOD retrieval possible. Second, ocean surfaces are generally more suitable for aerosol remote sensing due to the low reflectivity of water and the predominance of bright maritime aerosols. Exceptions happen in the presence of less scattering aerosols and lower zenith angles (e.g., biomass burning in the Gulf of Guinea).

4.1.3. Spectral Information

The different channels of geostationary imagers also provide varied information for aerosol remote sensing, as some sensing wavelengths may allow the retrieval that is not possible at others. This is common to polar orbiting satellites equipped with multi-spectral imagers. For example, the results reported in Section 3.5.1 show that the low sensitivity to aerosols observed for the MSG channel VIS06 over the Sahel region may be overcome if longer wavelengths are considered. The distinct information provided along the spectral dimension will be further exploited by the future MTG-I mission thanks to the new channels of the FCI imager. For example, results show that the sensing of fine aerosols over the Amazon Forest and Northern Europe may be improved thanks to the FCI channel VIS04, which does not exist for SEVIRI (see Figure 12). Similarly, the new channel IR022 may also help with the detection of coarser particles. This additional potential of MTG-I may help to improve the detection of aerosols [13] and to enhance chemical transport models through data assimilation [12]. Similar wavelengths to those of the two FCI channels considered in this work are already available for the Himawari-8/9 and GOES-16/17 platforms.

4.2. Limitations

Some limitations may impact the results reported in the present article. For example, the quality of the information on aerosol type may be limited in some cases due to the potential uncertainties in CAMS reanalysis and the conversion of CAMS aerosol components to OPAC aerosol types. Similarly, the surface albedo derived from the MDAL product may present some inaccuracies for some regions where aerosol correction is challenging (e.g., desert areas). Furthermore, the Lambertian assumption that is made for surface reflectivity could impact the results obtained for the diurnal study. Finally, some static parameters that are considered in the radiative transfer simulations may not be representative for all Meteosat observations. For example, a different content in water vapor, than the one in the U.S. standard atmosphere 1976 used in this study, may play on the properties of aerosols through their hygroscopic nature [54]. Additionally, the impact of a different height distribution of aerosols, than the one in the OPAC aerosol types [39] used in this work, was not investigated. All these limitations were considered to be minor and acceptable for the goal of the article, which aims to provide a qualitative but reliable overview of the potential of geostationary satellites for AOD retrieval.

4.3. Implications to Remote Sensing and Future Directions

The outcomes of this work provide useful information for studies on aerosols based on geostationary remote sensing. The conclusions on the variable sensitivity of spaceborne observations to aerosols according to the changes in CSA can be used to quantify the quality of satellite AOD products. Moreover, studies on surface remote sensing can also benefit from this work. While aerosol remote sensing becomes difficult for conditions close to CSA, the estimation of surface albedo is no longer limited to the existing AOD uncertainties in this situation [55].

The current study may also be also helpful in the design of retrieval algorithms for meteorological satellites. For example, dCSA may be used to weight the satellite observations according to its suitability for aerosol detection prior to their inversion. The value of dCSA could be also linked to the uncertainty of AOD retrievals, which is a key parameter for conducting aerosol studies [56,57]. Finally, the correlation between CSA and SSA shown in Figure 5d could be exploited to derive the latter parameter, as it was pointed out by Seidel and Popp [32]. Future research will be carried out in these directions.

Another outcome of the present work is the possibility of filling the gaps that arise when retrievals are not possible (i.e., due to low dCSA) at some instants of the day. Gap-filling methods could be applied to extrapolate the AOD retrievals resulting from favorable observations (i.e., due to high dCSA) of the same day. This extrapolation should be possible since aerosol conditions do not often change much in the short time scales (i.e., below a few hours) [58]. However, the retrieval of AOD at different times of the day requires the accurate knowledge of the aerosol phase function, which is often not known with a high degree of precision.

Parallel to the work presented in previous sections, an additional effort was done to allow the scientific community to calculate CSA without the need of performing radiative transfer simulations. Polynomial equations were derived from the regression of the CSA look-up table. The use of these simple equations in retrieval methods may be more efficient than using a large LUT. The outcomes of this experiment are reported in Appendix A.

5. Conclusions

Remote sensing from space is a unique tool to study atmospheric aerosols at the regional and global scales. However, the success of aerosol retrieval from space depends on the sensing parameters, such as satellite geometry, aerosol type, and surface reflectivity. This study exploited the concept of critical surface albedo to determine the potential of geostationary observations for the determination of the AOD depending on the observed region, the time of the day, the season, and the sensing wavelength. This potential was measured by means of the difference between the observed surface albedo and the corresponding CSA (referred to as dCSA), which is intimately linked to the sensitivity of spaceborne observations to the AOD. The better conditions for aerosol retrieval were found for observations far away from the satellite local noon when low scattering angles result in a higher aerosol signal. One exception happens for regions close to the sub-satellite point with overlaying coarse aerosols. In this case, the back-scattering peak of aerosols allows their detection at the local noon when scattering angle is high. Potential for aerosol retrieval also increases for seasons when the excursion of the geometry during the day is significant, which enhances the chances to obtain observations with suitable geometry for AOD retrieval. The varying feasibility during the day to detect aerosols that is made possible by geostationary satellites can be exploited for the commonly challenging bright surfaces (e.g., deserts and urban areas). Regarding the spatial coverage of geostationary satellites, the outer edge of the disk obtains higher values of dCSA thanks to their low scattering angle. However, the enhanced sensitivity to AOD observed in this region may be impacted as one goes to the limb by the loss of spatial resolution and the viewing of more air mass. Oceans generally show a higher sensitivity to aerosols due to the greater contrast between the surface and the aerosols. Finally, a higher potential in terms of dCSA is reported for the retrieval of fine particles using short wavelengths (lower than 0.5 microns) over vegetation surfaces and coarse particles using long wavelengths (higher than 1.5 microns) over bare soil regions. These results were obtained based on one year of maps of dCSA calculated for MSG and MTG-I observations. However, this work can be extrapolated to other geostationary satellites such as GOES-16/17 and Himawari-8/9. Another outcome of this work is the derivation of simple equations to calculate CSA without the need of performing costly radiative transfer simulations. The information provided in this study using the CSA concept can be used to refine aerosol retrieval algorithms and to estimate the quality of satellite-derived aerosol products.

Author Contributions: Conceptualization, X.C.; Data curation, S.M.; Formal analysis, X.C. and S.M.; Funding acquisition, X.C. and D.C.; Investigation, X.C. and S.M.; Methodology, X.C., S.M. and F.C.S.; Software, S.M.; Supervision, X.C. and D.C.; Visualization, S.M.; Writing – original draft, X.C.; Writing – review & editing, X.C., S.M., D.C. and F.C.S.

Funding: This research was partially supported by EUMETSAT, contract number EUM/RSP/SOW/17/963965. Part of this research was carried out at the Jet Propulsion Laboratory, California Institute of Technology, under a contract with the National Aeronautics and Space Administration (80NM0018D004).

Acknowledgments: We acknowledge the ICARE Data and Services center for providing the SEVIRI data that were used in this study. The SAF LSA and the SAF NWC are thanked for their SEVIRI-derived cloud mask and surface albedo, respectively. The ECMWF is acknowledged for providing the CAMS aerosol reanalysis. The libRadtran team is thanked for helping with the use of their radiative transfer tool. Josef Gasteiger is acknowledged for his support on using the MOPSMAP package. Finally, Chloé Vincent is thanked for fruitful discussions.

Conflicts of Interest: The authors declare no conflicts of interest.

Appendix A

The LUT of CSA values generated in Section 2.3 was fitted using an ordinary least squares multi-regression approach. Geometries corresponding to Meteosat observations were given a larger weight for the fitting. The regression method allowed the expression of the CSA using a linear combination of simple terms depending on the view and solar geometry of each observation

$$\begin{aligned}\mathrm{CSA} = a + b\cos(\xi) + c\cos(\xi)^2 + d\exp(-1/\mu_s) + e\exp(-1/\mu_v) + f\cos(\xi)\exp(-1/\\ \mu_v) + g\cos(\xi)^2\exp(-1/\mu_v) + h\exp(-1/\mu_s)\exp(-1/\mu_v),\end{aligned} \tag{A1}$$

where ξ is the scattering angle, μ_s is the cosine of the SZA, and μ_v is the cosine of the VZA. This multiple regression was carried out for aerosol types *continental_average*, *desert*, and *maritime_clean* and for channel VIS06. Regression coefficients are given in Table A1, as well as the statistics of the fit (i.e., average correlation, bias, and root mean square error).

Table A1. Multi-regression coefficients for channel VIS06 and fitting scores.

	continental_average	*desert*	*maritime_clean*
a	0.492	0.543	0.660
b	0.526	0.812	1.137
c	0.409	0.954	1.308
d	−0.540	−0.858	−0.586
e	−0.792	−0.865	−0.994
f	−0.747	−0.512	−0.969
g	−0.609	−0.729	−0.789
h	1.709	2.678	2.665
R-value	0.973	0.908	0.915
Bias	0.000	0.000	0.000
RMSE	0.013	0.048	0.061

References

1. Boucher, O.; Randall, D.; Artaxo, P.; Bretherton, C.; Feingold, G.; Forster, P.; Kerminen, V.-M.; Kondo, Y.; Liao, H.; Lohmann, U.; et al. Clouds and Aerosols. In *Climate Change 2013: The Physical Science Basis. Contribution of Working Group I to the Fifth Assessment Report of the Intergovernmental Panel on Climate Change*; Stocker, T.F., Qin, D., Plattner, G.-K., Tignor, M., Allen, S.K., Boschung, J., Nauels, A., Xia, Y., Bex, V., Midgley, P.M., Eds.; Cambridge University Press: Cambridge, UK; New York, NY, USA, 2013.
2. Kaufman, Y.; Tanré, D.; Boucher, O. A satellite view of aerosols in the climate system. *Nature* **2002**, *419*, 215–223. [CrossRef] [PubMed]
3. King, M.D.; Dubovik, O. Determination of aerosol optical properties from inverse methods. In *Aerosol Remote Sensing*; Lenoble, J., Remer, L., Tanré, D., Eds.; Springer: Berlin/Heidelberg, Germany, 2013; pp. 13–51.
4. Laszlo, I.; Ciren, P.; Liu, H.; Kondragunta, S.; Tarpley, J.D.; Goldberg, M.D. Remote sensing of aerosol and radiation from geostationary satellites. *Adv. Space Res.* **2008**, *41*, 1882–1893. [CrossRef]
5. Timmermans, R.M.; Schaap, M.; Builtjes, P.; Elbern, H.; Siddans, R.; Tjemkes, S.; Vautard, R. An Observing System Simulation Experiment (OSSE) for Aerosol Optical Depth from Satellites. *J. Atmos. Oceanic Technol.* **2009**, *26*, 2673–2682. [CrossRef]
6. Castellanos, P.; Da Silva, A.M.; Darmenov, A.S.; Buchard, V.; Govindaraju, R.C.; Ciren, P.; Kondragunta, S. A Geostationary Instrument Simulator for Aerosol Observing System Simulation Experiments. *Atmosphere* **2019**, *10*, 2. [CrossRef]
7. Goto, D.; Kikuchi, M.; Suzuki, K.; Hayasaki, M.; Yoshida, M.; Nagao, T.M.; Choi, M.; Kim, J.; Sugimoto, N.; Shimizu, A.; et al. Aerosol model evaluation using two geostationary satellites over East Asia in May 2016. *Atmos. Res.* **2019**, *217*, 93–113. [CrossRef]
8. Schmetz, J.; Pili, P.; Tjemkes, S.; Just, D.; Kerkmann, J.; Rota, S.; Ratier, A. An Introduction to Meteosat Second Generation (MSG). *Bull. Am. Meteorol. Soc.* **2002**, *83*, 977–992. [CrossRef]
9. Schmit, T.J.; Gunshor, M.M.; Menzel, W.P.; Gurka, J.J.; Li, J.; Bachmeier, A.S. Introducing the next generation Advanced Baseline Imager on GOES-R. *Bull. Am. Meteorol. Soc.* **2005**, *86*, 1079–1096. [CrossRef]
10. Bessho, K.; Date, K.; Hayashi, M.; Ikeda, A.; Imai, T.; Inoue, H.; Kumagai, Y.; Miyakawa, T.; Murata, H.; Ohno, T.; et al. An introduction to Himawari-8/9 - Japan's new-generation geostationary meteorological satellites. *J. Meteorol. Soc. Jpn. Ser. II* **2016**, *94*, 151–183. [CrossRef]
11. Klaes, K.D. An update on EUMETSAT programmes and plans. In *Earth Observing Systems XXIII*; International Society for Optics and Photonics: San Diego, CA, USA, 2018; Volume 10764.
12. Descheemaecker, M.; Plu, M.; Marécal, V.; Claeyman, M.; Olivier, F.; Aoun, Y.; Blanc, P.; Wald, L.; Guth, J.; Sič, B.; et al. Monitoring aerosols over Europe: An assessment of the potential benefit of assimilating the VIS04 measurements from the future MTG/FCI geostationary imager. *Atmos. Meas. Technol.* **2019**, *12*, 1251–1275. [CrossRef]
13. Aoun, Y. Évaluation de la sensibilité de l'instrument FCI à bord du nouveau satellite Meteosat Troisième Génération imageur (MTG-I) aux variations de la quantité d'aérosols d'origine désertique dans l'atmosphère. Ph.D. Thesis, MINES ParisTech, PSL - Research University, Sophia Antipolis, France, 2016.

14. Knapp, K.R.; Vonder Haar, T.H.; Kaufman, Y.J. Aerosol optical depth retrieval from GOES-8: Uncertainty study and retrieval validation over South America. *J. Geophys. Res.* **2002**, *107*, AAC-2. [CrossRef]
15. Prados, A.I.; Kondragunta, S.; Ciren, P.; Knapp, K.R. GOES Aerosol/Smoke Product (GASP) over North America: Comparisons to AERONET and MODIS observations. *J. Geophys. Res.* **2007**, *112*, D15201. [CrossRef]
16. Carrer, D.; Roujean, J.-L.; Hautecoeur, O.; Elias, T. Daily estimates of aerosol optical thickness over land surface based on a directional and temporal analysis of SEVIRI MSG visible observations. *J. Geophys. Res. Atmos.* **2010**, *115*, D10208. [CrossRef]
17. Govaerts, Y.M.; Wagner, S.; Lattanzio, A.; Watts, P. Joint retrieval of surface reflectance and aerosol optical depth from MSG/SEVIRI observations with an optimal estimation approach: 1. Theory. *J. Geophys. Res.* **2010**, *115*, D0220. [CrossRef]
18. Wagner, S.C.; Govaerts, Y.M.; Lattanzio, A. Joint retrieval of surface reflectance and aerosol optical depth from MSG/SEVIRI observations with an optimal estimation approach: 2. Implementation and evaluation. *J. Geophys. Res.* **2010**, *115*, D02204. [CrossRef]
19. Zhang, H.; Lyapustin, A.; Wang, Y.; Kondragunta, S.; Laszlo, I.; Ciren, P.; Hoff, R.M. A multi-angle aerosol optical depth retrieval algorithm for geostationary satellite data over the United States. *Atmos. Chem. Phys.* **2011**, *11*, 11977–11991. [CrossRef]
20. Carrer, D.; Ceamanos, X.; Six, B.; Roujean, J.-L. AERUS-GEO: A newly available satellite-derived aerosol optical depth product over Europe and Africa. *Geophys. Res. Lett.* **2014**, *41*, 7731–7738. [CrossRef]
21. *GOES-R Advanced Baseline Imager (ABI) Algorithm Theoretical Basis Document For Suspended Matter/Aerosol Optical Depth and Aerosol Size Parameter*; Version 4.2; NOAA Nesdis Center for Satellite Applications and Research: Grand Forks, ND, USA, 2018.
22. Yoshida, M.; Kikuchi, M.; Nagao, T.M.; Murakami, H.; Nomaki, T.; Higurashi, A. Common retrieval of aerosol properties for imaging satellite sensors. *J. Meteor. Soc. Jpn.* **2018**, *96B*, 193–209. [CrossRef]
23. Shi, S.; Cheng, T.; Gu, X.; Letu, H.; Guo, H.; Chen, H.; Wu, Y. Synergistic Retrieval of Multi-temporal Aerosol Optical Depth over North China Plain Using Geostationary Satellite Data of Himawari-8. *J. Geophys. Res. Atmos.* **2018**, *123*, 5525–5537. [CrossRef]
24. Govaerts, Y.; Luffarelli, M. Joint retrieval of surface reflectance and aerosol properties with continuous variation of the state variables in the solution space—Part 1: Theoretical concept. *Atmos. Meas. Tech.* **2018**, *11*, 6589–6603. [CrossRef]
25. Luffarelli, M.; Govaerts, Y. Joint retrieval of surface reflectance and aerosol properties with continuous variation of the state variables in the solution space – Part 2: Application to geostationary and polar-orbiting satellite observations. *Atmos. Meas. Tech.* **2019**, *12*, 791–809. [CrossRef]
26. Gupta, P.; Levy, R.C.; Mattoo, S.; Remer, L.A.; Holz, R.E.; Heidinger, A.K. Retrieval of aerosols over Asia from the Advanced Himawari Imager: Expansion of temporal coverage of the global Dark Target aerosol product. *Atmos. Meas. Tech. Discuss.* **2019**. [CrossRef]
27. Lenoble, J.; Mishchenko, M.I.; Herman, M. Absorption and Scattering by Molecules and Particles. In *Aerosol Remote Sensing*; Lenoble, J., Remer, L., Tanré, D., Eds.; Springer: Berlin/Heidelberg, Germany, 2013; pp. 13–51.
28. Fraser, R.; Kaufman, Y. The Relative Importance of Aerosol Scattering and Absorption in Remote Sensing. *IEEE Trans. Geosci. Remote Sens.* **1985**, *GE-23*, 625–633.
29. De Almeida Castanho, A.D.; Vanderlei Martins, J.; Artaxo, P. MODIS Aerosol Optical Depth Retrievals with high spatial resolution over an Urban Area using the Critical Reflectance. *J. Geophys. Res.* **2008**, *113*, D02201. [CrossRef]
30. Zhu, L.; Martins, J.V.; Remer, L.A. Biomass burning aerosol absorption measurements with MODIS using the critical reflectance method. *J. Geophys. Res.* **2011**, *116*, D07202. [CrossRef]
31. Wells, K.C.; Martins, J.V.; Remer, L.A.; Kreidenweis, S.M.; Stephens, G.L. Critical reflectance derived from MODIS: Application for the retrieval of aerosol absorption over desert regions. *J. Geophys. Res.* **2012**, *117*, D03202. [CrossRef]
32. Seidel, F.C.; Popp, C. Critical surface albedo and its implications to aerosol remote sensing. *Atmos. Meas. Tech.* **2012**, *5*, 1653–1665. [CrossRef]
33. Boehmler, J.M.; Loría-Salazar, S.M.; Stevens, C.; Long, J.D.; Watts, A.C.; Holmes, H.A.; Barnard, J.C.; Arnott, W.P. Development of a Multispectral Albedometer and Deployment on an Unmanned Aircraft for Evaluating Satellite Retrieved Surface Reflectance over Nevada's Black Rock Desert. *Sensors* **2018**, *18*, 3504. [CrossRef]

34. Cochrane, S.P.; Schmidt, K.S.; Chen, H.; Pilewskie, P.; Kittelman, S.; Redemann, J.; LeBlanc, S.; Pistone, K.; Kacenelenbogen, M.; Segal Rozenhaimer, M.; et al. Above-Cloud Aerosol Radiative Effects based on ORACLES 2016 and ORACLES 2017 Aircraft Experiments. *Atmos. Meas. Tech. Discuss.* **2019**. [CrossRef]
35. Zhang, Q.; Shia, R.-L.; Sander, S.P.; Yung, Y.L. XCO2 retrieval error over deserts near critical surface albedo. *Earth Space Sci.* **2016**, *3*, 36–45. [CrossRef]
36. Mayer, B.; Kylling, A. Technical note: The libRadtran software package for radiative transfer calculations - description and examples of use. *Atmos. Chem. Phys.* **2005**, *5*, 1855–1877. [CrossRef]
37. Emde, C.; Buras-Schnell, R.; Kylling, A.; Mayer, B.; Gasteiger, J.; Hamann, U.; Kylling, J.; Richter, B.; Pause, C.; Dowling, T.; et al. The libRadtran software package for radiative transfer calculations (version 2.0.1). *Geosci. Model Dev.* **2016**, *9*, 1647–1672. [CrossRef]
38. Anderson, G.P.; Clough, S.A.; Kneizys, F.X.; Chetwynd, J.H.; Shettle, E.P. *AFGL Atmospheric Constituent Profiles (0–120 km)*; AFGL-TR-86-0110; Air Force Geophysics Laboratory, Hanscom Air Force Base: Bedford, MA, USA, 1986; 43p.
39. Hess, M.; Koepke, P.; Schult, I. Optical Properties of Aerosols and Clouds: The Software Package OPAC. *Bull. Am. Meteorol. Soc.* **1998**, *79*, 831–844. [CrossRef]
40. Gasteiger, J.; Wiegner, M. MOPSMAP v1.0: A versatile tool for the modeling of aerosol optical properties. *Geosci. Model Dev.* **2018**, *11*, 2739–2762. [CrossRef]
41. Lefèvre, M.; Oumbe, A.; Blanc, P.; Espinar, B.; Gschwind, B.; Qu, Z.; Wald, L.; Schroedter-Homscheidt, M.; Hoyer-Klick, C.; Arola, A.; et al. McClear: A new model estimating downwelling solar radiation at ground level in clear-sky conditions. *Atmos. Meas. Tech.* **2013**, *6*, 2403–2418. [CrossRef]
42. Geiger, B.; Carrer, D.; Franchisteguy, L.; Roujean, J.-L.; Meurey, C. Land Surface Albedo Derived on a Daily Basis From Meteosat Second Generation Observations. *IEEE Trans. Geosci. Remote Sens.* **2008**, *46*, 3841–3856. [CrossRef]
43. Carrer, D.; Roujean, J.-L.; Meurey, C. Comparing operational MSG/SEVIRI land surface albedo products from Land SAF with ground measurements and MODIS. *IEEE Trans. Geosci. Remote Sens.* **2010**, *48*, 1714–1728. [CrossRef]
44. Samain, O.; Geiger, B.; Roujean, J.-L. Spectral normalization and fusion of optical sensors for the retrieval of BRDF and albedo: Application to VEGETATION, MODIS, and MERIS data sets. *IEEE Trans. Geosci. Remote Sens.* **2006**, *44*, 3166–3179. [CrossRef]
45. Feng, Y.; Liu, Q.; Ying, Q.; Liang, S. Estimation of the ocean water albedo from remote sensing and meteorological reanalysis data. *IEEE Trans. Geosci. Remote Sens.* **2016**, *54*, 850–868. [CrossRef]
46. Proud, S.R.; Fensholt, R.; Rasmussen, M.O.; Sandholt, I. A comparison of the effectiveness of 6S and SMAC in correcting for atmospheric interference of Meteosat Second Generation images. *J. Geophys. Res.* **2010**. [CrossRef]
47. Jones, H.M.; Crosier, J.; Russel, A.; Flynn, M.J.; Irwin, M.; Choularton, T.W.; Coe, H.; McFiggans, G. In situ aerosol measurements taken during the 2007 COPS field campaign at the Hornisgrinde ground site. *Q. J. R. Meteorol. Soc.* **2011**, *137*, 252–266. [CrossRef]
48. Dramé, M.S.; Ceamanos, X.; Roujean, J.L.; Boone, A.; Lafore, J.P.; Carrer, D.; Geoffroy, O. On the Importance of Aerosol Composition for Estimating Incoming Solar Radiation: Focus on the Western African Stations of Dakar and Niamey during the Dry Season. *Atmosphere* **2015**, *6*, 1608–1632. [CrossRef]
49. Adesina, A.J.; Kumar, K.R.; Sivakumar, V. Variability in aerosol optical properties and radiative forcing over Gorongosa (18.97°S, 34.35°E) in Mozambique. *Meteorol. Atmos. Phys.* **2015**, *127*, 217–228. [CrossRef]
50. Bozzo, A.; Remy, S.; Benedetti, A.; Flemming, J.; Bechtold, P.; Rodwell, M.J.; Morcrette, J.-J. *Implementation of a CAMS-Based Aerosol Climatology in the IFS*; Technical Memorandum, Research Department, ECMWF: Reading, England, 2017.
51. Ba, M.B.; Nicholson, S.E.; Frouin, R. Satellite-derived surface radiation budget over the African continent. Part II: Climatologies of the various components. *J. Clim.* **2001**, *14*, 60–76. [CrossRef]
52. Menut, L.; Flamant, C.; Turquety, S.; Deroubaix, A.; Chazette, P.; Meynadier, R. Impact of biomass burning on pollutant surface concentrations in megacities of the Gulf of Guinea. *Atmos. Chem. Phys.* **2018**, *18*, 2687–2707. [CrossRef]
53. Derrien, M.; Le Gleau, H. MSG/SEVIRI cloud mask and type from SAFNWC. *Int. J. Remote Sens.* **2005**, *26*, 4707–4732. [CrossRef]

54. Zieger, P.; Fierz-Schmidhauser, R.; Weingartner, E.; Baltensperger, U. Effects of relative humidity on aerosol light scattering: Results from different European sites. *Atmos. Chem. Phys.* **2013**, *13*, 10609–10631. [CrossRef]
55. Moparthy, S.; Carrer, D.; Ceamanos, X. Can we detect the browness or greenness of the Congo rainforest using satellite-derived surface albedo? A study on the role of aerosol uncertaintites. *Suistainability* **2019**, *11*, 1410. [CrossRef]
56. Witek, M.L.; Garay, M.J.; Diner, D.J.; Bull, M.A.; Seidel, F.C. New approach to the retrieval of AOD and its uncertainty from MISR observations over dark water. *Atmos. Meas. Tech.* **2018**, *11*, 429–439. [CrossRef]
57. Sayer, A.M.; Govaerts, Y.; Kolmonen, P.; Lipponen, A.; Luffarelli, M.; Mielonen, T.; Patadia, F.; Popp, T.; Povey, A.C.; Stebel, K.; et al. A review and framework for the evaluation of pixel-level uncertainty estimates in satellite aerosol remote sensing. *Atmos. Meas. Tech. Discuss.* **2019**. [CrossRef]
58. Anderson, T.L.; Charlson, R.J.; Winker, D.M.; Ogren, J.A.; Holmén, K. Mesoscale Variations of Tropospheric Aerosols. *J. Atmos. Sci.* **2003**, *60*, 119–136. [CrossRef]